Guided-Wave Intensity Modulators Using Amplitude-and-Phase Perturbations

RICHARD A. SOREF, SENIOR MEMBER, IEEE, DONALD L. McDANIEL, JR., AND BRIAN R. BENNETT

Abstract—**A theoretical analysis of intensity modulation in coupled waveguides and Mach–Zehnder interferometers is reported. Simultaneous phase and amplitude perturbations $\Delta n + i\Delta k$ are considered. Predictions are made about the performance of electrooptic GaAs and InP modulators controlled by the free-carrier effect (ΔN) or by the Franz–Keldysh effect (ΔE). The phase-dominant condition $\Delta n > 5\Delta k$ is optimal. The predicted depth of modulation is greater than that of conventional loss-modulators over a range of ΔN or ΔE.**

I. Introduction

GROUP IV and III-V semiconductors exhibit carrier-induced and field-induced electrooptic effects. The applied stimulus produces a simultaneous change in the semiconductor's optical attenuation and phase retardation. At certain wavelengths, the loss and phase components are comparable in size. These facts have been generally ignored in the design of optical intensity modulators. This paper explores the use of combined amplitude-and-phase modulation for enhanced intensity modulation. Coupled waveguides and Mach–Zehnder interferometers are examined.

In the past, guided-wave intensity modulation has been obtained with either the Pockels effect or the Franz–Keldysh effect. Pockels devices are usually operated at an optical wavelength λ far from the fundamental absorption edge of the material λ_g. There, phase effects are strong and the associated loss is negligible. By contrast, Franz–Keldysh devices are operated quite near the edge. For those modulators, device engineers have relied solely on the loss component and have chosen to overlook the relatively weak phase retardation. This paper deals with an intermediate spectral region, further from the edge, where the phase-and-amplitude variations have similar magnitudes. Carrier-controlled and field-controlled devices are analyzed. We predict that the resulting modulators will have higher extinction ratios and lower insertion losses than conventional "straight through" loss modulators.

Unlike conventional Franz–Keldysh modulators that have a background absorption of 25–50 cm^{-1}, the modulators proposed here have a static loss of less than 1 cm^{-1} which should allow monolithic integration of our modulators with other guided-wave components (including laser diodes) on the same wafer.

Manuscript received March 11, 1987; revised August 12, 1987.

The authors are with the Rome Air Development Center, Solid-State Sciences Directorate, Hanscom AFB, MA 01731.

IEEE Log Number 8718499.

II. Background Discussion

Van Eck and coworkers [1] studied the Franz–Keldysh effect in bulk GaAs and InP. They suggested that the loss-and-phase components could be combined in a bulk-optic Fabry–Perot resonator for improved modulation. We have applied their idea to two integrated-optic structures and have considered carrier control.

Previously, researchers have employed four types of guided-wave devices to convert phase variations into intensity modulation: 1) interferometers, 2) coupled waveguides, 3) mode extinction modulators, and 4) TE-to-TM mode converters. Here, we have generalized 1) and 2) to include optical "damping". Modulators 3) and 4) are not treated in this paper, but are promising candidates for future study.

In the analysis below, the complex mode-amplitude for the propagation-direction z is described by the expression $A_0 \exp i(\omega t - \kappa z)$. If we include the effect of optical loss, then the complex wavenumber κ is proportional to the complex index of refraction: $\kappa = 2\pi(n + ik)/\lambda$, where the real part ($n$) is the conventional refractive index and the imaginary part (k) is the linear extinction coefficient. We define the propagation coefficient as $\beta = 2\pi n/\lambda$ and the optical power absorption coefficient as $\alpha = 4\pi k/\lambda$. The units of both α and β are per centimeter. We are interested in electrooptic effects that produce a complex change in index: $\Delta \boldsymbol{n} = \Delta n + i\Delta k$. This produces a mode perturbation of the form $\exp i(\Delta\beta + i\Delta\alpha/2)z$, where

$$\Delta\beta = 2\pi\Delta n/\lambda, \qquad \Delta\alpha = 4\pi\Delta k/\lambda.$$

The analysis below is quite simplified. For example, interfering modes are treated like plane waves. Also, we assume that the transverse index distribution $\Delta \boldsymbol{n}(x, y)$ is uniform and fills the optical waveguide. The response of coupled three-dimensional (3-D) channel waveguides is deduced from the behavior of coupled two-dimensional (2-D) slab waveguides.

III. Modulator Structures

Fig. 1 illustrates the three single-mode channel waveguide structures that are analyzed here: in Fig. 1(a) a straight segment of waveguide with variable attenuation, in 1(b) a Mach–Zehnder interferometer made from Y-couplers, and in 1(c) a pair of parallel coupled channels with uncoupled input and output lead-in channels. In all three devices, electrical control is imposed upon an interaction

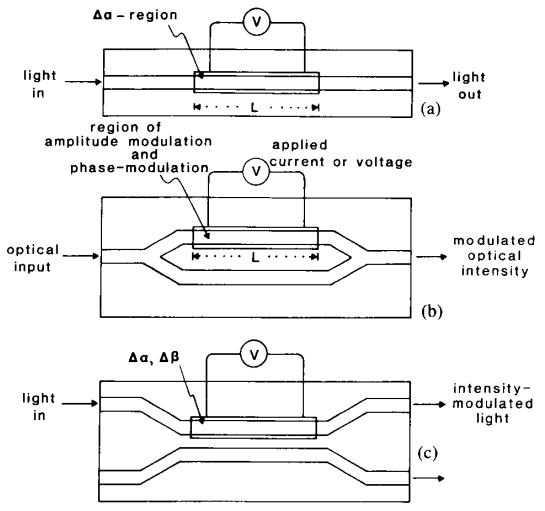

Fig. 1. Three types of electrooptic guided-wave modulators: (a) absorbing channel, (b) Mach-Zehnder interferometer, (c) coupled waveguides. Types (b) and (c) use simultaneous phase-and-amplitude perturbations.

region of length L to produce a uniform perturbation of the waveguide $\Delta\beta + i\Delta\alpha/2$ over that length. Only one arm is perturbed in Fig. 1(b) and (c). We assume that the guide pair is phase matched in the zero field case, when $\Delta\beta = 0$ and $\Delta\alpha = 0$. This is the lossless initial state of the device in Fig. 1(b) or (c). The final state is reached when the electrooptic effect gives a velocity mismatch $\Delta\beta + i\Delta\alpha/2$ between the guides.

We shall compute the normalized optical output power P_{out}/P_{in} in the three cases. For the conventional Fig. 1(a) modulator, it is clear that

$$P_{out}/P_{in} = e^{-\Delta\alpha L}. \tag{1}$$

A phase retardation $\exp(i\Delta\beta L)$ is present but does not contribute to intensity change. Turning to the Fig. 1(b) interferometer, we have $P_{out} \sim E_t E_t^*$, where E_t is the total optical field at the Y-combiner. Here, $E_t = A_0/\sqrt{2} + (A_0/\sqrt{2}) \exp(-\Delta\alpha L/2) \exp(i\Delta\beta L)$; thus

$$P_{out} = (A_0^2/2)[1 + e^{-\Delta\alpha L/2}e^{i\Delta\beta L}][1 + e^{-\Delta\alpha L/2}e^{-i\Delta\beta L}]. \tag{2}$$

At zero perturbation, constructive interference occurs since the path length is the same in each arm. Then, the transmission is a maximum: $2A_0^2$. Taking $P_{in} = 2A_0^2$, we obtain from (2) the throughput of the interferometer:

$$P_{out}/P_{in} = (1/4)[1 + e^{-\Delta\alpha L} + 2e^{-\Delta\alpha L/2} \cos \Delta\beta L]. \tag{3}$$

Analogous equations with $\Delta\alpha$ and $\Delta\beta$ can be developed for Fabry-Perot and Michelson interferometers.

Consider now the Fig. 1(c) device. We shall analyze the case in which an optical amplitude A_0 is launched into the "feed" waveguide, while an amplitude B_0 is launched into the "branch" waveguide. Output amplitudes A and B from feed and branch, respectively, are calculated. One has the option of inserting the electrooptic perturbation in either the feed or branch. (The reason for not putting identical perturbations in feed and branch is given below). We shall label the inputs ports of the coupler as 1 and 2, and designate the output ports as 3 and 4. The normalized output powers are: $P_3/P_1 = |A/A_0|^2$, $P_4/P_1 = |B/A_0|^2$, $P_3/P_2 = |A/B_0|^2$, and $P_4/P_2 = |B/B_0|^2$. The initial condition $B_0 = 0$ is assumed below.

Coupled-mode equations for a uniform $\Delta\beta$-switch have been given in several textbooks such as Yariv and Yeh [2]. Those equations were derived under the assumptions of weak coupling, phase-matched guides, slab waveguides, and codirectional propagation. The uniform coupling coefficient is K per centimeter.

To handle the combined phase and amplitude shift, we have substituted the complex quantity $\Delta\beta + i\Delta\alpha/2$ for $\Delta\beta$ everywhere in the standard coupled-mode equations (e.g., see [2, sect. 6.4, eq. (30) and (31)]) with the following result:

$$P_3/P_1 = e^{-\Delta\alpha L/2} \left|\cos gL + i(b/g) \sin gL\right|^2 \tag{4}$$

$$P_4/P_1 = e^{-\Delta\alpha L/2} \left|i(K/g) \sin gL\right|^2 \tag{5}$$

where

$$g^2 = b^2 + K^2$$

and

$$b = \pm(\Delta\beta/2 + i\Delta\alpha/4).$$

The justification for this procedure is given in the recent work of Thompson [3] who considered coupled guides that include gain or loss. In fact, Thompson's result [3, eq. (7)] connects with our result if we interpret his static gain/loss parameter $2K\delta$ as our "dynamic" amplitude perturbation $\Delta\alpha/4$, and his phase shift $2K\Delta\beta$ as our phase mismatch $\Delta\beta/2$.

In (4) and (5) above, the plus sign in b denotes a perturbation in the feed, while the minus sign indicates a branch perturbation. Note that g is complex. For this modulator, we shall select a value of KL that gives either an initial crossover of light (the "cross" state, with $KL = \pi/2, 3\pi/2, 5\pi/2, \cdots$) or an initial straight-through condition (the "bar" state, with $KL = \pi, 2\pi, 3\pi, \cdots$).

A key parameter in the present theory is the ratio

$$\rho = \Delta n/\Delta k = 2\Delta\beta/\Delta\alpha. \tag{6}$$

This ρ-parameter provides a measure of the relative strength of the phase versus the amplitude modulation at a given drive level. The $\Delta n/\Delta k$ ratio is also useful in assessing the amount of chirp in the modulator [4]. The effect of ρ on P_{out}/P_{in} is now determined. We have a choice of using either $\Delta\alpha L$ or $\Delta\beta L$ as the independent variable. To be specific, if we put (6) into (3) we find the response of the Mach-Zehnder (M-Z) is:

$$P_{out}/P_{in} = (1/4)[1 + e^{-\Delta\alpha L} + 2e^{-\Delta\alpha L/2} \cos(\rho\Delta\alpha L/2)]. \tag{7}$$

Alternatively, we find

$$P_{out}/P_{in} = (1/4)[1 + e^{-2\Delta\beta L/\rho} + 2e^{-\Delta\beta L/\rho}\cos(\Delta\beta L)]. \quad (8)$$

Turning to the directional coupler (lc), we shall take $KL = m\pi$ as the boundary condition and use (4)–(6) to give

$$P_3/P_1 = e^{-\Delta\alpha L/2}\left|\cos gL \pm [(\rho + i)(\Delta\alpha L)/(4gL)]\sin gL\right|^2 \quad (9)$$

$$P_4/P_1 = e^{-\Delta\alpha L/2}\left|(im\pi/gL)\sin gL\right|^2 \quad (10)$$

where

$$(gL)^2 = (\rho + i)^2(\Delta\alpha L/4)^2 + (m\pi)^2.$$

Alternatively, we find:

$$P_3/P_1 = e^{-\Delta\beta L/\rho}\left|\cos gL \pm [(i - 1/\rho)(\Delta\beta L)/(2gL)]\sin gL\right|^2 \quad (11)$$

$$P_4/P_1 = e^{-\Delta\beta L/\rho}\left|(im\pi/gL)\sin gL\right|^2 \quad (12)$$

where

$$(gL)^2 = (1 + i/\rho)^2(\Delta\beta L/2)^2 + (m\pi)^2.$$

Feed and branch perturbations produce the same result for P_4/P_1, according to (10) and (12).

It is possible to place a perturbation of length L in both guides in Fig. 1(b) and 1(c), which has been done in the past for Pockels-effect devices. Unlike push–pull Pockels devices that give $+\Delta\beta$ in one arm and $-\Delta\beta$ in the other, the Franz–Keldysh and charge-controlled devices give the same sign of $\Delta\beta$ in both arms. Hence, the phase-velocity mismatch will vanish in the voltage-on state. This implies that the phase terms will cancel in the above equations and that only the loss terms will remain. Thus, we find that the modulator with two active arms has a throughput of $P_{out}/P_{in} = \exp(-\Delta\alpha L)$ in Fig. 1(b) and (c).

In the sections below, we shall compare the complex modulators with both phase-sensitive and amplitude-sensitive devices.

IV. Comparison With $\Delta\beta$ Devices

In the past, the coupler and the M–Z have been used with the Pockels effect, a "pure phase" perturbation. So, these structures can serve as phase-modulated references for the complex modulator in the limit of large ρ. As ρ is increased, the mixed modulator must blend continuously into the phase modulator. The "blending" is shown graphically below. In the following computations, we shall assume that ρ is a constant. Fig. 2 is a plot (per (8)) of the M–Z output as a function of $\Delta\beta L$ for $\rho = 3$, 10, and 5000 ($\rho \to \infty$). The familiar raised cosine result at $\rho \to \infty$ with perfect nulls at odd multiples of π is seen. The complex modulator has nonzero minima and nonunity maxima because, with increasing Δk, the amplitude imbalance between the two arms washes out the peaks and valleys of the interference "pattern". However, the intensity minima and maxima of the complex device occur

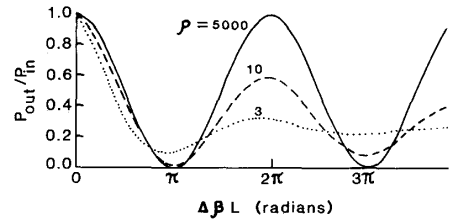

Fig. 2. Interferometer output as a function of electrooptic phase angle (real part of perturbation) for three values of $\Delta n/\Delta k$.

at the same values of π, 2π, 3π, etc. (slightly left-shifted at low ρ). In the high-field limit (large $\Delta\beta L$), the optical throughput of the mixed interferometer approaches the asymptote 1/4. This is explained as follows. In the limit of large $\Delta\beta L$, assuming that Δn and Δk increase in unison, one arm of the interferometer becomes opaque, so half the power is lost. In addition, the large amplitude imbalance and phase imbalance of the optical signals entering the Y-combiner will cause half of the remaining power to be radiated into the substrate [5].

Fig. 3 shows the responses P_3/P_1 and P_4/P_1 of a 2 × 2 coupler switch (equations (11) and (12)) as a function of $\Delta\beta L$ for $\rho = 5$, 15, and 5000 with an initial cross state, $KL = \pi/2$. For the upper drawing, the complex perturbation is in the feed. A companion plot, lower drawing, shows the effect of a branch perturbation. The $\rho = 5000$ device reaches the bar state at the well-known value $\Delta\beta L = \sqrt{3}\pi$. The quasibar state of the $\Delta n + i\Delta k$ devices occurs at the same $\Delta\beta L$ value, although the outputs differ from the ideal unity/zero values.

Next, we considered the initial bar state, $KL = \pi$. Fig. 4 presents results for P_3/P_1 and P_4/P_1 versus $\Delta\beta L$ for a feed perturbation (upper drawing) and for a branch perturbation (lower drawing). Again, we examined $\rho = 5$ (dotted line), 15 (dashed line), and 5000 (solid line). It is interesting that the $\rho = 5000$ device becomes a ~3-dB coupler at $\Delta\beta L = 2\pi$.

Some insight into the mixed-modulator curves of Figs. 3 and 4 can be gained from a consideration of the phase-only coupler. For example, if we plot P_3/P_1 versus L for a phase-only coupler (as Thompson has done in [3, fig. 5]), we find the usual raised cosine result at $\Delta\beta = 0$, with perfect ones and zeros that represent the bar and cross states. For the mismatched condition, the L-dependent output power oscillates between ~0.5 and unity when $\Delta\beta \sim 4K$. So, in the nonsynchronous condition, it is impossible to reach a perfect cross state, although any one of a series of bar states can be attained. We conclude that one can go from a perfect cross state at $\Delta\beta = 0$ to a perfect bar state at $\Delta\beta \neq 0$. But, a bar state at $\Delta\beta = 0$ will never lead to a perfect cross state at $\Delta\beta \neq 0$. Similar behavior holds for the phase-dominant mixed coupler shown in Figs. 3 and 4. In addition, the loss component $\Delta\alpha$ affects the coupled modes. One mode becomes more localized in the perturbed lossy guide, and its attenuation increases. The other mode becomes more localized in the transparent unperturbed guide, and its attenuation diminishes [3].

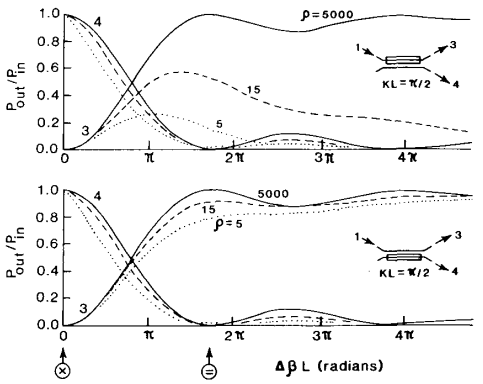

Fig. 3. Directional coupler output(s) as a function of electrooptic phase angle (real part of perturbation) for three values of $\Delta n/\Delta k$. The cross state is the initial condition.

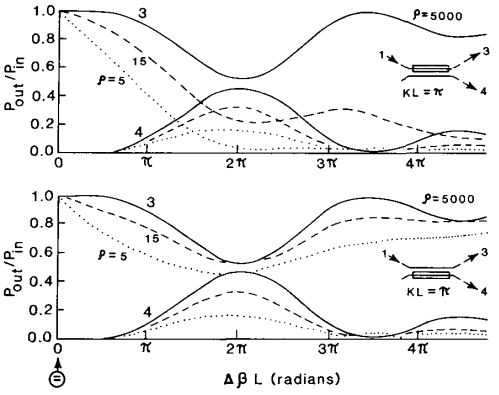

Fig. 4. Directional coupler output(s) as a function of electrooptic phase angle (real part of perturbation) for three values of $\Delta n/\Delta k$. The bar state is the initial condition.

In designing an intensity modulator, one selects the most highly damped output. That output is P_4/P_1 in Fig. 3 (feed or branch perturbation) and P_3/P_1 in Fig. 4 (feed perturbation). The collective action of $\Delta\alpha$ and $\Delta\beta$ is different in these two situations. In Fig. 3, increasing $\Delta\beta$ drives P_4/P_1 "downwards" towards the bar state at 1.73π. This tendency is reinforced by the increased damping $\Delta\alpha$ which attenuates the cross coupled optical power. The situation is reversed in Fig. 4. Here, the phase component $\Delta\beta$ drives P_3/P_1 to ~ 0.5 as $\Delta\beta L$ approaches 2π. Then, P_3/P_1 is driven "upwards" to unity at $\Delta\beta L = 3.5\pi$. But, the $\Delta\alpha$ component acts directly on P_3/P_1 and drives that power towards zero, thereby opposing the $\Delta\beta$ effect. So, the $\Delta\alpha$-effect is diluted. For these reasons, the intensity modulation is more effective in Fig. 3 than in Fig. 4.

V. Comparison With $\Delta\alpha$ Devices

The straight-through attenuator of Fig. 1(a) is now used as a reference for Fig. 1(b) and (c). In practice, the straight

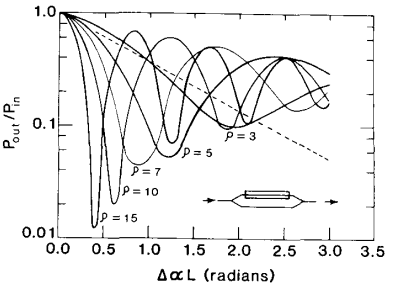

Fig. 5. Interferometer output as a function of electrooptic "amplitude angle" (imaginary part of perturbation) for five values of $\Delta n/\Delta k$.

device is always used with a complex $\Delta n + i\Delta k$ perturbation because there is no such thing as a "pure loss" perturbation. So, it is fair to compare Fig. 1(a) with Fig 1(b) and (c) because all three are complex. On the other hand, the straight device is an inefficient modulator in the sense that its Δn-component does not contribute to intensity modulation. The performance advantage of Fig. 1(b and (c) over (a), shown below, is due to the concerted action of Δn and Δk. To facilitate the comparison, we shall assume that the modulators are controlled by the variable $\Delta\alpha L$. Starting with the M–Z, we have shown in Fig 5 the predicted performance (equation (7)) versus $\Delta\alpha L$ for $\rho = 3$, 5, 7, 10, and 15 in a semilog plot. For comparison, the response of the exp $(-\Delta\alpha L)$ modulator is shown by the dashed line. Note that the horizontal scale is not in units of π. The conclusion drawn from Fig. 5 is that the interferometer gives better extinction than the conventional device when $\Delta\alpha L$ is kept below 1.65 for $\rho = 5$, below 1.30 for $\rho = 7$, 0.95 for $\rho = 10$, and 0.65 for $\rho = 15$. When $\Delta\alpha L$ exceeds those critical values, the M–Z has less depth-of-modulation than the in-line modulator.

Fig. 6 illustrates the coupler behavior. This figure represents the theoretical performance (equation (9) and (10)) versus $\Delta\alpha L$ for the case $KL = \pi/2$ and $\rho = 20$. This mixed coupler is a 2×2 switch with unequal outputs in the bar state. There is a deep minimum of P_4/P_1 (bar state) at $\Delta\alpha L = 0.54$ which is $2\sqrt{3}\,\pi/\rho$.

Fig. 7 and 8 are semilog plots of one output (equations (10) and (9), respectively) as a function of $\Delta\alpha L$. Results for $\rho = 2$, 5, 10, 15, and 20 are shown. Fig. 7 presents P_4/P_1 for $KL = \pi/2$ (feed or branch perturbation), and Fig. 8 shows P_3/P_1 for $KL = \pi$ (feed perturbation). For comparison, the response of the exp $(-\Delta\alpha L)$ absorption modulator is shown by the dashed line. For $\rho > 5$ in Fig. 7, the curves are well below the dashed line, as desired. We conclude from Fig. 7 that the phase-dominant condition $\Delta n > 5\Delta k$ is well suited for efficient intensity modulation. In Fig. 8, the output power oscillates about the dashed line and does not offer a significant improvement over the conventional loss modulator for reasons given above.

We have examined the loss-dominant regime, $\rho = 0.5$, and have found that the $\rho = 0.5$ curves (not shown) are

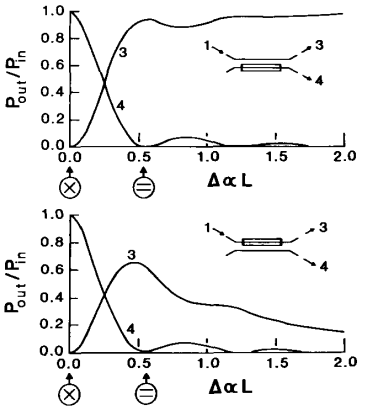

Fig. 6. Directional coupler output(s) as a function of electrooptic amplitude angle (imaginary part of perturbation) for $\Delta n = 20\Delta k$. The cross state is the initial condition.

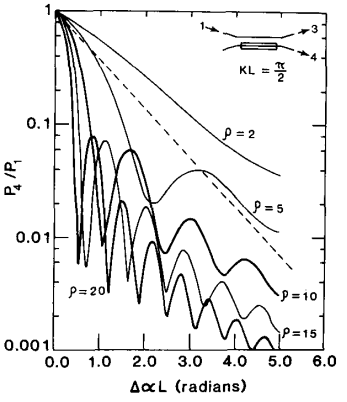

Fig. 7. Directional coupler output (branch waveguide) as a function of electrooptic amplitude angle (imaginary part of perturbation) for five values of $\Delta n/\Delta k$. The cross state is the initial condition.

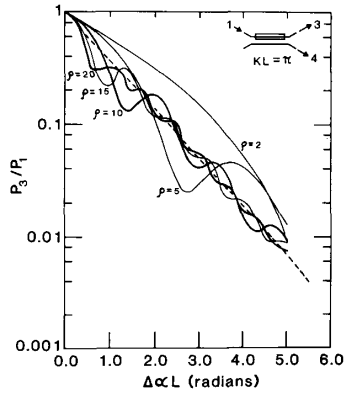

Fig. 8. Directional coupler output (feed waveguide) as a function of electrooptic amplitude angle (imaginary part of perturbation) for five values of $\Delta n/\Delta k$. The bar state is the initial condition.

above the dashed line in Figs. 7 and 8, so we conclude that the loss-dominant regime is not favorable in the coupler. A similar conclusion applies to the M-Z.

VI. Electrooptic Effects

In a III-V semiconductor, the Pockels, Franz–Keldysh, and free-carrier electrooptic effects coexist over a range of wavelengths. However, it is possible to isolate one effect, that is, to emphasize one and diminish the others. This can be done by choosing an appropriate crystallographic orientation, electrical contact structure, doping, wavelength, etc. In order to gauge the individual impact of each effect upon modulation, we shall examine the Franz–Keldysh and charge effects separately.

The optical influence of altered free-carrier densities (ΔN) in Ge, Si, GaAs, InP, InAs, etc., has been discussed in the literature as the "plasma dispersion effect." The real and imaginary parts of this effect are called carrier refraction (*CR*) and carrier absorption (*CA*), respectively. For GaAs, InP, and Si, some experimental and theoretical results on $\Delta\alpha$ and $\Delta\beta$ as a function of ΔN have been plotted in [6, figs. 2 and 3]. The combined *CR* and *CA* effects, designated here as $C(R + A)$ are strongest away from the edge: $\lambda >> \lambda_g$.

The ratio ρ for $C(R + A)$ can be estimated using the simple Drude model cited in [7, eqs. (4) and (5)]. For one species of carrier, the model gives $\rho = -2\pi cm^*\mu/e\lambda$, where m^* is the conductivity effective mass, and μ the carrier mobility. For most materials, experiments have verified a linear dependence of $\Delta\beta$ upon ΔN at "high" ΔN. However, $\Delta\alpha$-measurements reveal that $\Delta\alpha$ is a nonlinear function of ΔN, although the deviation from linearity is small. Thus, in practice, ρ is not independent of ΔN, but the variation of ρ with ΔN is smaller than the 1000-to-1 change of ρ with E in the Franz–Keldysh effect. In the $C(R + A)$ effect, one has an opportunity to "tailor" ρ to a desired value by the proper choice of semiconductor material, alloy composition, optical wavelength, maximum ΔN, and species of carrier (electrons or holes). However, ρ is constrained by the dispersion relations [6]. The $C(R + A)$ effect is polarization-independent.

To illustrate $C(R + A)$, the example of hole-injection into GaAs will be given. From room-temperature GaAs at the 1.15-μm wavelength, Carenco and Menigaux [8] cite experimental absorption work by Garmire and Merz, and theoretical refractive index work by Stern. For free holes, they find that $\Delta\alpha(\text{cm}^{-1}) = 1.4 \times 10^{-17}\Delta N_h(\text{cm}^{-3})$ and $\Delta n = -9.9 \times 10^{-22}\Delta N_h(\text{cm}^{-3})$, which implies that $\Delta\beta(\text{cm}^{-1}) = -5.4 \times 10^{-17}\Delta N_h(\text{cm}^{-3})$. These results are plotted in Fig. 9 as a function of injected hole density. It is seen that the ratio ρ is constant at 7.7, although other data on GaAs suggests that ρ tends to decrease with increasing ΔN. (For electrons in InP or GaAs, ρ is typically greater than 10 in the near infrared). Generally, as ΔN is increased from 10^{16} to 10^{19} cm^{-3} in Si, Ge, GaAs, and InP, we expect ρ to

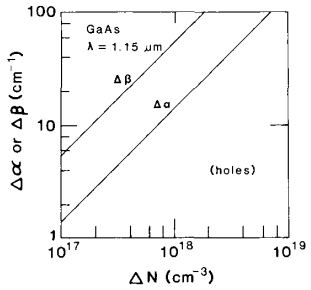

Fig. 9. Carrier-induced optical phase shift and induced optical absorption in GaAs produced by a modulation ΔN of the free-hole concentration ($\lambda = 1.15\ \mu$m and $\lambda_g = 0.88\ \mu$m).

decrease by a factor of five (approximately), tracking the decrease in mobility.

The real and imaginary parts of the Franz-Keldysh effect are called electrorefraction (ER) and electroabsorption (EA), respectively. These effects were examined theoretically for direct-gap III-V materials by Bennett and Soref [9] and for an indirect-gap material (Si) in [7]. In the transparent region $\lambda > \lambda_g$, it is found that the phase-part increases approximately quadratically with the external electric field, $\Delta\beta = bE^2$ at low E, while the electroabsorption has a much stronger field-dependence: $\Delta\alpha \propto E^7$ at low fields, changing to $\propto E^5$ and $\propto E^3$ with increasing field. The $E(R + A)$ effect peaks as the modulator wavelength λ approaches the edge of the waveguide material λ_g, although one must not approach the edge too closely in order to minimize the zero-field extinction k_0 of the modulator. That loss arises from absorption-band tails.

In the $E(R + A)$ effect, the relative size of $\Delta\beta$ and $\Delta\alpha$ can be adjusted by proper choice of: semiconductor material, $\lambda - \lambda_g$, maximum E-field, crystallographic orientation, electrode placement, propagation direction, alloy composition, and layer thicknesses (in multiple-quantum-well samples). For the discussion below, we shall assume that the electrode placement and crystallographic orientation are chosen so that the Pockels effect is smaller than $E(R + A)$, although one can obtain comparable Δn-contributions from the linear and nonlinear electrooptic effects, if desired. The $E(R + A)$ effect is polarization-dependent.

Fig. 10 illustrates $E(R + A)$ for room-temperature InP material at the 0.984-μm wavelength. The quantities Δn and Δk have been plotted as a function of applied field in Fig. 10 (a log-log plot) using the theoretical curves of [9]. Here, the photon energy has been chosen to be 80 meV less than the bandgap energy. The 80-meV choice is advantageous because it reduces the background extinction at $E = 0$ to a low level: $k_0 \sim 3 \times 10^{-6}$. For use in numerical examples below, the ratio $2\Delta\beta/\Delta\alpha$ and the amplitude modulation $\Delta\alpha$ are plotted versus E in the semilog plot of Fig. 11.

VII. Predicted Performance

Three examples of intensity modulation are given here: $E(R + A)$ in Fig. 1(b) and (c), and $C(R + A)$ in Fig. 1(c). Applying the carrier effect in GaAs to the coupled waveguides of Fig. 7, we note that $\rho = 7.7$ from Fig. 9. Then we select a practical value of ΔN, such as 5×10^{17} cm^{-3}, as a convenient starting point. Fig. 9 indicates that $\Delta\alpha = 7.0$ cm^{-1} at this ΔN. Next, we note from the Fig. 7 result that the minimum value of P_4/P_1 for $\rho = 7.7$ occurs at $\Delta\alpha L = 1.4$ approximately. Thus, the required interaction length is $1.4/7.0$, that is, $L = 0.20$ cm. It also follows that the coupling coefficient is $\pi/2(0.2)$ or 7.9 cm^{-1}. Next, we let ΔN vary from zero to 7×10^{17} cm^{-3} and determine the corresponding $\Delta\alpha L$ values, which are inserted into (10) along with the fixed ρ value. This gives the modulation result shown in Fig. 12 as a function of the injected (or depleted) charge concentration. Also displayed on the graph, for comparison, is a dashed-line curve that illustrates the response of the conventional absorption modulator.

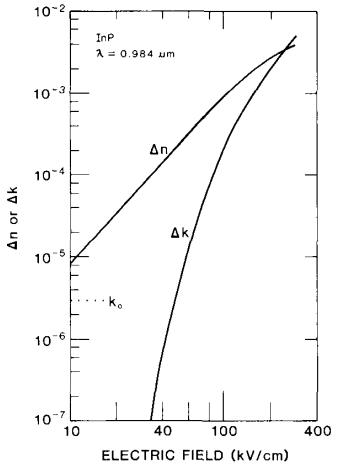

Fig. 10. Franz-Keldysh refractive-index perturbation and added optical extinction in InP induced by an external electric field ($\lambda = 0.984\ \mu$m, and $\lambda_g = 0.925\ \mu$m).

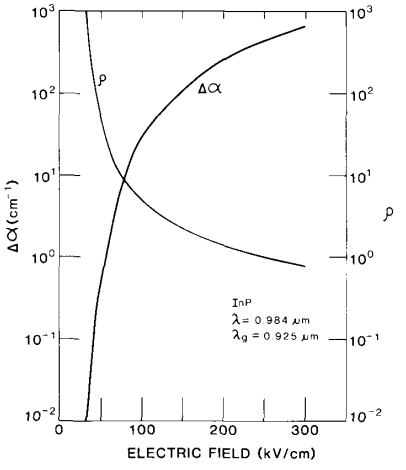

Fig. 11. Field-induced optical absorption and the ratio $\Delta n/\Delta k$ in InP as a function of applied field (curves derived from Fig. 10).

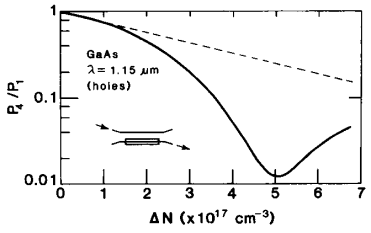

Fig. 12. Optical intensity modulation in coupled GaAs waveguides (per Fig. 7) versus carrier injection/depletion, as produced by the Fig. 9 electrooptic effect. Here, $K = 7.9\ \text{cm}^{-1}$ and $L = 0.200$ cm.

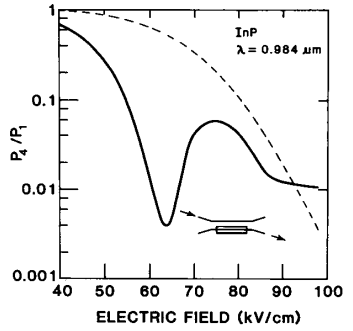

Fig. 13. Optical intensity modulation in coupled InP waveguides (per Fig. 7) versus applied field, as produced by the Fig. 10 electrooptic effect. Here, $K = 6.7\ \text{cm}^{-1}$ and $L = 0.233$ cm.

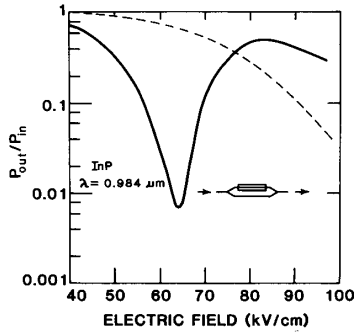

Fig. 14. Optical intensity modulation in an InP interferometer (per Fig. 5) versus applied field, as produced by the Fig. 10 electrooptic effect. Here, $L = 0.133$ cm.

The second coupled-waveguide example makes use of the field-controlled $E(R + A)$ effect in InP at a photon energy 80 meV less than the bandgap energy, i.e., an operating wavelength of 0.984 μm. Again we take $KL = \pi/2$. It is estimated from Fig. 7 that when $\rho = 15$, the first minimum of P_4/P_1 occurs at $\Delta\alpha L = 0.7$. (The choice $\rho = 15$ is one of several practical alternatives). Turning to Fig. 11, we then find that $\rho = 15$ occurs at a field strength of 66 kV/cm, where $\Delta\alpha = 3.0\ \text{cm}^{-1}$ also occurs. The required interaction length in this case is 0.7/3.0, that is, $L = 0.233$ cm. Hence, $K = 6.7\ \text{cm}^{-1}$. Now, we select an operating range of field values from zero to 100 kV/cm. At each E value, we determine from Fig. 11 the corresponding ρ-value and the corresponding $\Delta\alpha L$ value. The various $\rho(E)$ and $\Delta\alpha L(E)$ are then substituted into (10) for determination of the P_4/P_1-versus-E modulation characteristic. The result is presented in Fig. 13. Again, for comparison, we show the throughput of the standard exp $(-\Delta\alpha L)$ modulator by the dashed curve.

The final example includes the response of the Mach–Zehnder interferometer to the $E(R + A)$ effect in InP at 0.984 μm. Here, we turn to the result of Fig. 5 and find that the ratio $\rho = 15$ gives a low value of $P_{\text{out}}/P_{\text{in}}$ at a relatively low value of $\Delta\alpha L$, namely at $\Delta\alpha L = 0.4$. From the InP result of Fig. 11, it is found that $\rho = 15$ corresponds to an electric field strength of 66 kV/cm. The absorption perturbation $\Delta\alpha = 3.0\ \text{cm}^{-1}$ corresponds to that field. The interaction length needed is 0.4/3.0, or $L = 0.133$ cm. Now we allow E to range from zero to 100 kV/cm. At each E-value, we find from Fig. 11 the corresponding ρ value and the $\Delta\alpha L$ value. Those numbers are substituted into (7) to give the optical throughput of the interfering guides. The result is presented as a function of E in Fig. 14. As before, we compare the result with the transmission of a conventional loss modulator (dashed curve).

Estimates of the optical insertion loss in each of the above three examples will now be made. The zero-field loss in decibels of the mixed modulator, either coupler or M–Z, is given approximately by -10 log [exp $(-4\pi k_0 L/\lambda)$]. Taking $k_0 = 3 \times 10^{-6}$ for InP at 0.984 μm and $k_0 \leq 1 \times 10^{-6}$ for GaAs at 1.15 μm, (extrapolated values from [10]) together with the 0.200, 0.233-, and 0.133-cm interaction lengths, we find that the insertion losses are only 0.1, 0.4, and 0.2 dB, respectively, for the Fig. 12–14 examples.

VIII. Discussion and Summary

The coupler and the M–Z will give effective intensity modulation when the complex electrooptic effect has a large phase component: $\Delta n > 5\Delta k$. Fig. 13 shows that the intensity falls to 0.0055 at 66 kV/cm (22.6-dB extinction, compared to 1-dB extinction for the reference, and the modulation depth is far greater than that of the reference over the 0-to-90 kV/cm range. Similarly, Fig. 12 reveals higher extinction than the reference over the ΔN range from 0 to $7 \times 10^{17}\ \text{cm}^{-3}$. In Fig. 14, the interferometer has better extinction than the reference modulator over the E-range from 0 to 76 kV/cm. The results of Figs. 12–14 are based on approximations discussed earlier. The results give qualitative guidelines for device behavior.

The Franz–Keldysh intensity modulator has a lumped-element equivalent electrical circuit, and driving the modulator is much like charging and discharging a capacitor. Modulation depth is governed by the electric field strength in the waveguide material, which in turn is proportional to the "capacitor voltage" (the reverse bias applied to the p-i-n waveguide diode structure). As shown in Figs. 2–4, the same $\Delta\beta L$ is used in the on-state of phase-dominant

and phase-only couplers (or interferometers). Thus, the switching power requirements are approximately the same for mixed and pure-phase devices.

Ordinary absorption modulators (Fig. 1(a)) tend to be operated in the loss-dominant regime where $\Delta n \cong \Delta k$. According to Fig. 10, the $\Delta n \leqq \Delta k$ condition requires higher field strengths and more switching energy than does the phase-dominant $\Delta n \geq 5\Delta k$ condition. However, the absorption modulator could be operated at a wavelength closer to λ_g than the mixed modulator. In that case, the conventional modulator might gain an advantage. In [9, figs. 8 and 9] it is shown that $\Delta n \cong \Delta k$ occurs at lower drive levels when $\lambda - \lambda_g$ shrinks. Hence, near λ_g, the switching power requirement of the absorption modulator might be one-half that of the mixed modulator, depending upon how small $\lambda - \lambda_g$ is. At the same time, however, the optical insertion loss of the absorption modulator would increase by several decibels because the background extinction coefficient goes up significantly as $\lambda - \lambda_g$ is reduced.

In summary, a theoretical analysis of intensity modulation is coupled waveguides and in Mach–Zehnder interferometers has been made. Simultaneous phase and amplitude perturbations $\Delta n + i\Delta k$ were considered. Performance predictions were made for electrooptic GaAs and InP modulators controlled by the free-carrier effect or by the Franz–Keldysh effect. The phase-dominant condition $\Delta n > 5\Delta k$ was optimal. The predicted depth of modulation was greater than that of conventional loss modulators over a prescribed range of charge densities or of field excursions.

References

[1] T. E. Van Eck, L. M. Walpita, W. S. C. Chang, and H. H. Wieder, "Franz-Keldysh electrorefraction and electroabsorption in bulk InP and GaAs," *Appl. Phys. Lett.*, vol. 48, pp. 451–453, 1986.

[2] A. Yariv and P. Yeh, *Optical Waves in Crystals*. New York: Wiley, 1986, p. 187.

[3] G. H. B. Thompson, "Analysis of optical directional couplers that include gain or loss, and their application to semiconductor slab dielectric guides," *J. Lightwave Technol.*, vol. LT-4, pp. 1678–1693, Nov. 1986.

[4] F. Koyama and K. Iga, "Frequency chirping of external modulator and its reduction," *Electron. Lett.*, vol. 21, p. 1065, 1985.

[5] H. J. Arditty, M. Papuchon, and C. Puech, "Reciprocity properties of a branching waveguide," in *Fiber Optic Rotation Sensors*, S. Ezekiel and H. Arditty, Ed. New York: Springer-Verlag, 1982, p. 102.

[6] R. A. Soref and B. R. Bennett, "Kramers–Kronig analysis of electrooptical switching in silicon," paper 704-07 in *Proc. 4th SPIE Integrated Optical Circuit Eng. Conf.* (Cambridge, MA), Sept. 18, 1986, vol. 704.

[7] R. A. Soref and B. R. Bennett, "Electrooptic effects in silicon," *IEEE J. Quantum Electron.*, vol. QE-23, pp. 123–129, Jan. 1987.

[8] A. Carenco and L. Menigaux, "GaAs homojunction rib waveguide directional coupler switch," *J. Appl. Phys.*, vol. 51, pp. 1325–1327, Mar. 1980.

[9] B. R. Bennett and R. A. Soref, "Electrorefraction and electroabsorption in InP, GaAs, GaSb, InAs, and InSb," *IEEE J. Quantum Electron.*, vol. QE-23, pp. 2159–2166, Dec. 1987.

[10] E. D. Palik, Ed. *Handbook of Optical Constants of Solids*. Orlando, FL: Academic, 1985.

*

Richard A. Soref (S'58–M'63–SM'71) received the B.S.E.E. and M.S.E.E. degrees from the University of Wisconsin in 1958 and 1959, and the Ph.D. degree in electrical engineering from Stanford University, Stanford, CA, in 1963.

From 1963 to 1965, he worked in the optics and infrared group of M.I.T.'s Lincoln Laboratory, Lexington, MA, and in 1965 he joined the Technical Staff of Sperry Research Center, Sudbury, MA, where he conducted research on a variety of topics including nonlinear optics, extrinsic-silicon infrared detectors, liquid crystal electrooptical devices, optical switching, and fiber-optic sensors. In November 1983, he joined the Rome Air Development Center, Hanscom AFB, MA, as a Research Scientist in the Solid State Sciences Directorate. His current interests include III-V and silicon integrated optics and microwave applications of optics. He has authored or coauthored 75 journal articles and holds 15 patents.

Dr. Soref is a member of the American Physical Society, the Society of Photo-Optical Instrumentation Engineers, and the Optical Society of America. He served as Chairman of the Boston Chapter IEEE Group on Electron Devices in 1969. He is currently an Editorial Advisor of *Optical Engineering*.

*

Donald L. McDaniel, Jr., was born in 1961. He was awarded the B.S.E.E. degree from Arizona State University, Tempe, AZ, in 1982, and the M.S.E.E. degree from Northeastern University, Boston, MA, in 1987.

He served as an officer in the U.S. Air Force from May 1982 through July 1987. His assignments included four years as a Fiber-Optics Technology Planning Officer in the Deputate for Development Plans of the USAF Electronics Systems Division, and one year as an Electrooptics Research Engineer in the Solid-State Sciences Directorate of the USAF Rome Air Development Center, Hanscom AFB, MA. He was serving in this last capacity during the time of this research. He is currently a Research Assistant at the University of New Mexico, Center for High Technology Materials, Albuquerque, NM, where he is pursuing the Ph.D. degree in optical sciences.

Mr. McDaniel is a member of the Society of Photo-Optical Instrumentation Engineers.

*

Brian R. Bennett was born in Kansas in 1962. He received the B.S. and M.S. degrees in geophysics from the Massachusetts Institute of Technology in 1984 and held both research and teaching assistantships. As an undergraduate, he conducted research on the induced polarization of minerals. His M.S. thesis investigated the conductivity of the earth's crust and upper mantle using simultaneous measurements of electric and magnetic fields (the magnetotelluric method).

He is currently serving in the U.S. Air Force in Bedford, MA, conducting research on low-temperature dielectric deposition and indium phosphide device technology. He has authored or coauthored ten journal articles and four presentations at technical meetings.

Mr. Bennett is a member of the Society for Optical Engineering, the Materials Research Society, the American Physical Society, and Sigma Xi.